Design of Highly Active Cobalt Catalysts for CO_2 Hydrogenation via the Tailoring of Surface Orientation of Nanostructures

Journal:	*Catalysis Science & Technology*
Manuscript ID	CY-ART-02-2019-000402
Article Type:	Paper
Date Submitted by the Author:	27-Feb-2019
Complete List of Authors:	Jimenez, Juan; University of South Carolina, Chemical Engineering Cun, Wen; University of South Carolina, Chemical Engineering Lauterbach, Jochen; University of South Carolina, Chemical Engineering

SCHOLARONE™
Manuscripts

Design of Highly Active Cobalt Catalysts for CO_2 Hydrogenation via the Tailoring of Surface Orientation of Nanostructures

Juan D. Jimenez, Cun Wen, and Jochen Lauterbach*

Department of Chemical Engineering, University of South Carolina, Columbia, SC 29208

Corresponding Author: lauteraj@cec.sc.edu

Abstract

The synthesis of nanomaterials with well-controlled morphologies and surface orientations has opened new avenues towards increasing catalytic performance and understanding of fundamental catalytic pathways. Here, we illustrate how tailoring surface orientations of Co_3O_4 catalysts on the nanoscale results in control over catalytic performance via the preferential formation of active surface species during CO_2 hydrogenation. This results in a significant increase in the methane yield on Co_3O_4 nanorods, as opposed to conventional nanoparticle catalysts, where Co_3O_4 nanorods inhibit the formation of formate spectator species via the preferential formation of bridged CO as an intermediate species. This design approach provides a new dimension for the development of next generation catalysts and opens new, more efficient strategies for the conversion of carbon dioxide into useful hydrocarbons.

Broader Context

Carbon dioxide utilization is an increasingly important chemical process as an alternative to carbon storage and capture due to the exponential increase in CO_2 emissions. Thermal-catalytic CO_2 hydrogenation is the most efficient means of converting CO_2 into a value-added product due to the ability to scale up the process to meet the large output of CO_2 production globally. Cobalt-based catalyst are often utilized for CO_2 hydrogenation due to their

high catalytic activity and the fact they are inexpensive compared to noble metals, such as ruthenium. In this work, cobalt catalysts were applied to CO_2 hydrogenation which utilize selective facet exposure to promote higher catalytic activity. The preferential exposure of the {110}/{001} family of surface facets via nanorod shaped cobalt was found to have a turnover frequency that was an order of magnitude higher than traditional spherical cobalt nanoparticles with selective exposure of the {111}/{001} family of surface facets. Our study showed that the cause for their differences in activity was due to the suppression of site blocking intermediates on the nanorods. In contrast, the nanoparticles yielded both the reactive intermediate, formyl, but also spectator species, formate, which ultimately caused the reduction in the observed catalytic activity.

1. Introduction

One promising route to mitigating CO_2 is converting point-source CO_2 into high-value chemicals, such as plastics or fuels. [1-5] A major hurdle resides in the high thermodynamic stability of CO_2, which leads to low reactivity.[3, 6, 7] Various catalytic routes taking CO_2 to value-added chemicals have been proposed, including photocatalytic, electrochemical, and direct thermocatalytic approaches.[3-5, 8] Amongst these proposed reactions, CO_2 hydrogenation is considered to be one of the most attractive due to its practical importance and potential for scale-up.[3, 7, 9, 10] The hydrogen required for the CO_2 hydrogenation reaction can be generated from renewable resources, such as biomass gasification, wind power, or solar water-splitting.[11-16]

Recent studies on the development of active catalysts for CO_2 hydrogenation are mainly focused on adjusting catalyst properties, such as particle size, oxidation states, and composition.[11-15] For example, Co catalysts with average particle sizes of 10 nm showed 3 times higher turnover frequency (TOF) than those with an average particle size of 3 nm.[17, 18] Rational design of catalyst structures on the nanoscale shows great potential toward increasing

the catalytic activity of CO_2 hydrogenation. The design of a catalyst based on a fundamental knowledge of the CO_2 hydrogenation reaction and first principles of surface science is important for cobalt based catalyst for CO_2 hydrogenation.[3] Many previous studies on the influence of catalyst structure on reactivity are typically based on bulk properties, which are not always consistent with those of the active surface.[19-21] The atomic structure and composition within the first few atomic layers of a surface is primarily responsible for the catalytic properties. Tuning the catalyst bulk structure will therefore not always result in a more active and selective catalyst. For instance, it is generally agreed that reduced Co on SiO_2 is about 4 times more active than oxidized Co for CO_2 hydrogenation.[12, 17, 22-24] Conversely, metallic Co on TiO_2 was shown to have up to 5 times lower activity than oxidized Co on the same support.[12] The mechanism of decreased activity due to Co reduction for the TiO_2 supported catalyst is not clear due to limited information on the surface structures of Co interacting with either TiO_2 or SiO_2 support. This example illustrates that tuning catalyst bulk properties (such as oxide vs. metal) without considering the intricacies of the surface structure can be misleading in the design of active catalysts.

Herein, we demonstrate that the existence of different surface facets on Co_3O_4 catalysts controls the catalytic activity of reduced Co catalysts for CO_2 hydrogenation, even when the catalysts exhibit very similar bulk properties, such as crystallographic phase, oxidation state, and chemical composition. Based on our recent work, the catalysts were synthesized by reducing faceted Co_3O_4 particles which serve as precursor state for the active metallic catalysts.[25, 26] These Co_3O_4 particles were obtained by controlling the catalyst morphology via a coprecipitation method,[25, 27] where cobalt nanorods with a {110}/{001} surface faceting were compared against traditional nanoparticles with {111}/{001} surface faceting. Bulk and surface structures were characterized with experimental techniques, including X-ray diffraction (XRD), Raman spectroscopy, and High-resolution transmission electron microscopy

(HRTEM). Furthermore, mechanistic understanding of the influence of the catalyst precursor surface faceting on catalytic performance was investigated with kinetic studies and *in situ* infrared (IR) spectroscopy during both CO_2 and CO hydrogenation, where the active surface species for CO_2 hydrogenation was selectively promoted over the {110}/{001} faceted nanorods, resulting in over an order magnitude greater catalytic activity for CO_2 hydrogenation than conventional nanoparticles.

2. Experimental Section

2.1 Synthesis of Co_3O_4 nanorods and nanoparticles

The Co_3O_4 nanorods were synthesized using a co-precipitation method by following previous literature reports.[27, 28] In a typical synthesis, $Co(OAc)_2 \cdot 4H_2O$ (4.98g; 99.999%, Sigma) was added to ethylene glycol (60mL; 99.8%, Sigma) under a N_2 (UHP, Airgas) atmosphere to remove residual O_2. The solution was then heated to 80 or 160 °C, for nanoparticles or nanorods; respectively. Afterward, an aqueous solution of Na_2CO_3 (200mL, 0.2 $mol \cdot L^{-1}$; 99.5% Sigma) was injected into the cobalt precursor solution at a rate of 1.11 mL min^{-1}. The mixture was further aged at the synthesis temperature for one more hour. The overhead solvent was decanted out and the solid product was collected via vacuum filtration and washing with ethanol. The filtered product was vacuum dried at 50 °C overnight, then calcined at 450°C for 4h.

2.2 Characterization Methods

X-Ray Diffraction was carried out with a Rigaku Miniflex II equipped with a Cu-Kα monochromatic X-ray source and a high-speed silicon strip detector. Pulse chemisorption experiments were carried out in a Micromeritics Autochem II 2920 unit using a TCD detector to monitor the CO uptake of the catalyst. All samples were dried then reduced at 450 ^oC for 5 hours and CO chemisorption was performed at 50 ^oC. Raman spectra were acquired using a

633nm laser source with a hole size of 1025µm, slit width of 300µm, and a grating of 950. The spectrometer was calibrated before each sample using a 520.7cm^{-1} silica standard with a tolerance of ±1.0cm^{-1}. Spectra were collected in an *in situ* Linkam cell using a flow rate of 20 mL min^{-1} of 4:1 ratio of H_2 to CO_2 after a 450^{o}C pretreatment under H_2 for 5 h.

2.3 in situ IR experiments

Two sets of *in situ* IR experiments were conducted on a Bruker Equinox 55 benchtop equipped with a Praying Mantis *in situ* diffuse reflectance Infrared Fourier transform (DRIFTS) cell to investigate the reactive species presented on the catalyst surface during CO_2 and CO hydrogenation. Before *in situ* IR experiments, Co nanorods and nanoparticles were reduced at 450 °C in flowing H_2 for 5h, then were cooled down to 250 °C. A background spectrum of the sample was taken with a resolution of 4 cm^{-1} under pure hydrogen. Once the temperature equilibrated, the reactant mixture of CO_2+ $4H_2$ or CO + $2H_2$ was introduced into the *in situ* DRIFT cell and the reaction was monitored at 250^{o}C at atmospheric pressure. Spectra were taken every 3-5 minutes to monitor surface species changing during reactions.

2.4 CO_2 catalytic hydrogenation

Generally, Co_3O_4 catalysts (0.3g) were mixed with sand (1.8g) using a 1:6 ratio of catalyst to sand in order to dissipate heat and then secured via quartz wool plugs inside the stainless-steel plug flow reactor. The catalysts were reduced at 450 °C with ultra-high purity H_2 (100mL·min^{-1}, 5h) before the catalytic tests of CO_2 hydrogenation. After reduction, the gas was switched from H_2 to a mixture of 18% CO_2, 72% H_2, and 10% Ar (custom mixture, Airgas), corresponding to a stoichiometric feed with the argon balance used as internal standard for the GC measurements. The gas hourly space velocity (GHSV) of the mixture gas was kept at 18,000 h^{-1} for all experiments. For experiments performed under a 2:1 ratio of H_2 to CO_2 the

gas mixture was 31% CO_2, 62% H_2 and 7% Ar (custom mixture, Airgas),. The catalytic activity and selectivity were measured while sweeping the reaction temperature between 100 °C to 400 °C with the rector pressure maintained at 10 bar. The products from CO_2 hydrogenation were analyzed on-line with a Shimadzu Gas Chromatograph GC2014 equipped with both thermo-conductivity (TCD) and flame ionization detectors (FID). The selectivity was calculated on a carbon basis. All catalytic tests were repeated using different batches of the designated catalyst to ensure reproducibility in both the synthesis and catalytic performance. This error is captured by the error bars displayed on the catalytic activity measurements. The carbon balance of all experimental runs closed within the experimental error of the GC measurements (95±7% carbon balance).

3. Results and Discussion

3.1 Catalytic Performance of Cobalt nanorods and nanoparticles

Cobalt oxide catalysts with either nanorod or nanoparticle morphologies were synthesized and tested for CO_2 hydrogenation.[26] It is generally believed that the active site for CO_2 hydrogenation is metallic Co.[29-33] During the reaction tests, the feed composition of H_2 and CO_2 was kept at the stoichiometric ratio of 4:1. Fig. 1 compares the catalytic activity for Co nanorods and nanoparticles. Co nanoparticles are used as a control group which is representative of a typical spherical cobalt catalyst, where the reaction rate between 220-400^{o}C of our Co nanoparticles (0.11-5.16x10^{-5} $mol_{CO2}\cdot g^{-1}\cdot s^{-1}$, respectively) is comparable to that reported for other Co catalysts (0.85-5.09×10^{-5} $mol_{CO2}\cdot g^{-1}\cdot s^{-1}$).[12] The Co nanorods show a reaction rate of 2.81x10^{-5} $mol_{CO2}\cdot g^{-1}\cdot s^{-1}$ at 220^{o}C, while the nanoparticles at the same

temperature show a rate of 3.94×10^{-6} $mol_{CO2}\cdot g^{-1}\cdot s^{-1}$. In addition, the nanorods begin to catalyze CO_2 hydrogenation at temperatures about 80°C lower than the Co nanoparticles. The selectivity to methane is maintained at 99±1% on the Co nanorods for all reaction temperatures, while it gradually increases from 13±1% to 95±2% on the Co nanoparticles with CO formed as a major product below 300°C. The hydrocarbon product distribution on both nanorods and nanoparticles contains over 90% of methane for all reaction conditions, with the remainder being C_2-C_5 (see supplemental Fig. 1). At 220 °C, the yield towards hydrocarbons is an order of magnitude greater than that on the nanoparticles. In fact, in the temperature range between 220 °C and 320 °C, the activity of the Co nanorods towards CO_2 hydrogenation is 3-17 times higher than that of the Co nanoparticles. The high activity and selectivity of Co nanorods was also maintained upon changing the ratio of H_2 : CO_2 from 4:1 to 2:1 (Supplementary Figure. 1). Even for these sub-stoichiometric feed conditions, the Co nanorods maintained a steady selectivity of 98±2 % towards methane over the entire temperature range, while the selectivity to hydrocarbons on the nanoparticles increased from 27±5 % to 92±4 % with increasing temperature. Lean H_2 conditions should be expected to favor CO over hydrocarbon production ($CO_2 + H_2 \rightarrow CO + H_2O$ vs. $CO_2 + 4H_2 \rightarrow CH_4 + 2H_2O$). Overall, not only do the cobalt nanorods show an order of magnitude greater reaction rate during CO_2 hydrogenation at identical operating conditions, the rods favor the complete reduction into methane while the nanoparticles only partially reduce the CO_2 into CO; this shows that the exposed faceting must play a fundamental role in altering not only the structure, but the reaction intermediates formed on the surface as well.

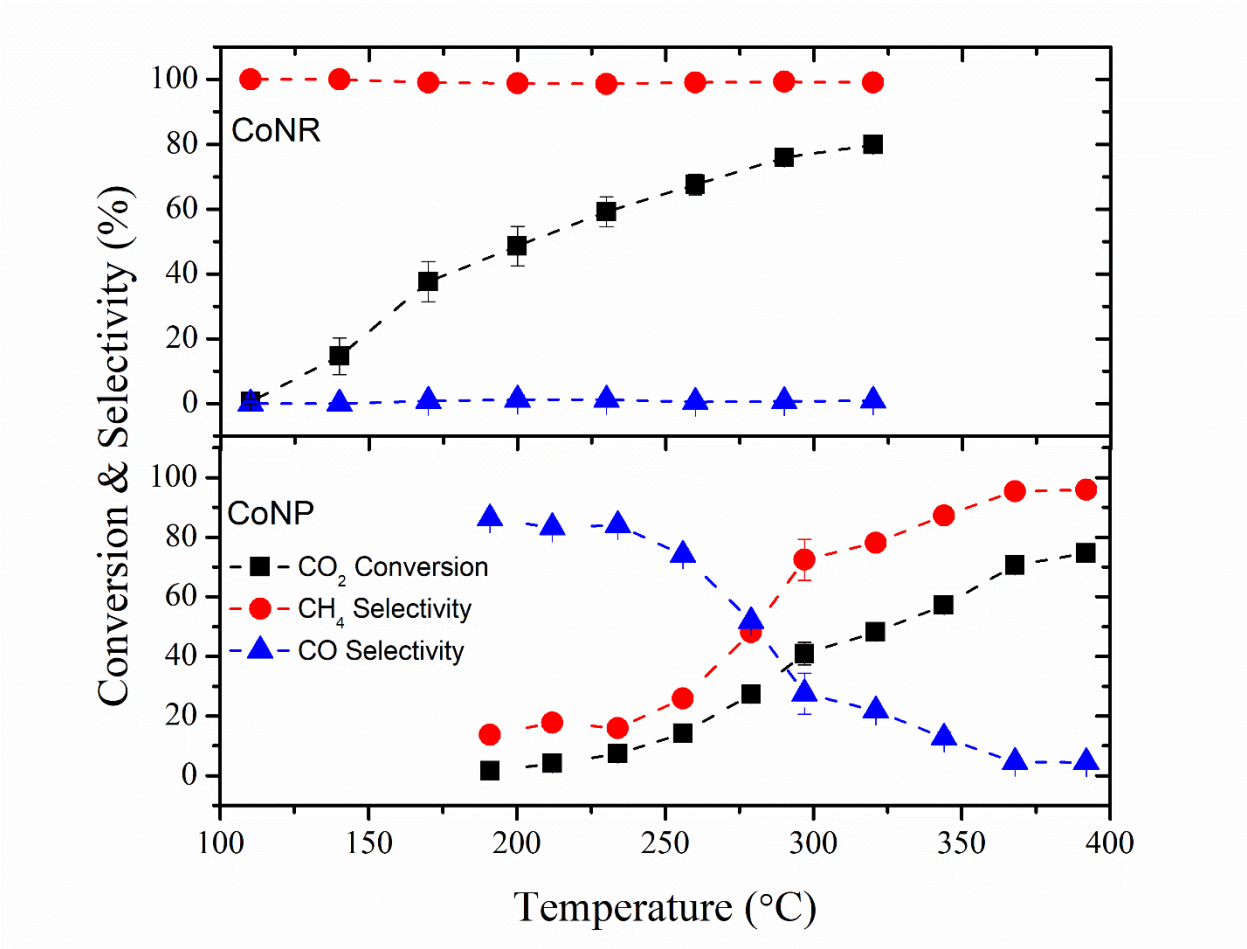

Figure 1. CO_2 conversion, hydrocarbon and CO selectivity, and hydrocarbon yield for Co nanorods and nanoparticles with a H_2 to CO_2 ratio of 4:1 at10 bar pressure and 18000 hr^{-1} flow

3.2 Particle size, structure and morphology

To study the influence of catalyst structure on catalytic performance, Co nanorods and Co nanoparticles were characterized with a variety of imaging and spectroscopic techniques. As shown in the TEM image in Fig. 2, the Co nanorods have a diameter of 14.2 ± 4.4 nm and lengths between 200 and 300 nm, which is consistent with our previous work.[25, 26] The Co nanoparticles have a particle size distribution of 24.5 ± 9.8 nm. The turnover frequency for

particle sizes above 10nm is expected to be independent of size for Co catalysts for CO_2 hydrogenation.[17, 30, 34]

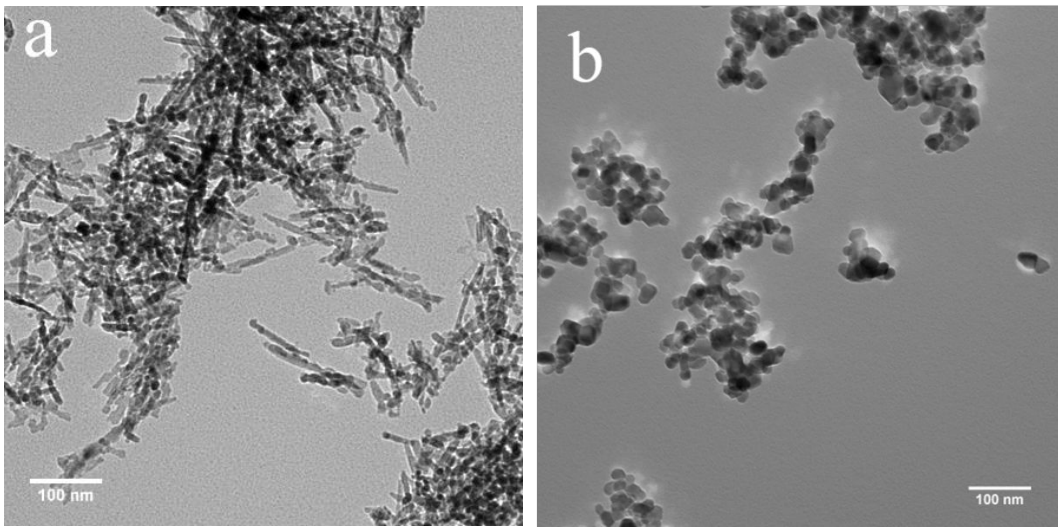

Figure 2. Transmission Electron Microscopy image of (a) cobalt nanorods and (b) cobalt nanoparticles after washing and calcining.

The crystal structures were determined by powder X-ray diffraction (XRD), as shown in supplemental Fig 2. The XRD peak positions and intensity ratios for both Co nanorods and nanoparticles are consistent with those of the Co_3O_4 spinel structure (PDF 41-1467). The grain size distribution via XRD for the nanorods and nanoparticles were 14.1 ± 2.4 nm and 28.5 ± 9.5 nm; respectively, which are within error of the measured size distribution via TEM. The grain size of the nanorods reflects the diameter of the nanorods measured via TEM, since during synthesis the nanorods grow preferentially along the [110] direction from the $Co_{x/2+y}(OH)_x(CO_3)_y$ precursor,[25, 27] forming continuous grains during its growth, whereas the nanoparticles grow uniformly along their radial axis resulting in grain sizes that are consistent with their actual particle size.

In a previous study we found that cobalt nanorods resist oxidation during Fischer-Tropsch synthesis with the addition of 10vol% H_2O to the feed, while cobalt nanoparticles were readily oxidized under the same conditions[26]. Given that the nanorods resisted oxidation, their improved catalytic activity towards CO_2 hydrogenation is most likely due to the preservation of the metallic cobalt phase during the reaction. Furthermore, bulk properties such as the particle size, crystal structure, and oxidation state of the prepared Co nanorods and nanoparticles are very similar. According to previous reports,[11-15, 17] these similarities between nanorods and nanoparticles should lead to comparable activity and selectivity for CO_2 hydrogenation. This shows that the catalyst bulk properties do not account for the observed differences in activity and selectivity differences, meaning a more detailed understanding of the catalytic surface is required.

3.3 Exposed surface structure via HRTEM

Aberration corrected-scanning transmission electron microscope (AC-STEM) equipped with a high angle annular dark field detector was used to characterize differences in surface properties between Co nanorods and nanoparticles. The AC-STEM images are shown in Fig. 3. The *d*-spacing measured for the Co nanorods was 2.9 ± 0.1 Å, which is consistent with the (220) plane of Co_3O_4 and results in the exposure of the {110} family of facets at the surface.[26] On the other hand, the *d*-spacing for the nanoparticles was measured to be 4.7 ± 0.1 Å, which corresponds to {111} and {001} family of facets exposed at the surface. The {110} family is the only surface orientation that has both Co^{2+} and Co^{3+} present in the outermost surface layer, while predominantly Co^{2+} is exposed on all the other facets.[26, 27] As both nanostructures share the {001} family of surface facets the effective surface area of the {110} and {111} can be compared when taken as the percentage of the total surface area for the nanorods and nanoparticles; respectively. The general geometry for the nanorods is taken to be rod shaped with flat ends and sides, while the nanoparticles are octahedrons with truncated

ends representing the {001} facets.[27] The relevant length scales from our TEM imaging was used to estimate the approximate percentage of surface facets; with an approximate diameter of 14 nm and a length of 200 nm for the nanorods and a diameter of 25 nm for the nanoparticles. The percentage of exposed {110} on the nanorods is approximately 39% while for the nanoparticles the percentage of exposed {111} is approximately 80%. Since the {001} family of surface facets does not possess the exposed Co^{3+} cations, it is considered to be less active than the {110} family of surface facets, however its contribution to the overall catalytic activity cannot be ruled out. Therefore, even though the Co nanorods and nanoparticles possess very similar bulk properties, the STEM images clearly show that they have different surface crystal facets and consequently expose different cations on the outmost, catalytically relevant surface. Direct imaging of the cobalt in the metallic state after a reduction could not be explored due to the highly oxophilic nature of cobalt. The use of environmental aberration correction transmission electron microscopy using a sufficiently high partial pressure of hydrogen to ensure reduction was not feasible. The presence of metallic cobalt as the catalytically relevant surface was verified via XPS, where the samples could be reduced in a pretreatment cell under the same pretreatment conditions used before the catalytic tests and then transferred under vacuum into the XPS measurement chamber, where the cobalt showed as completely reduced (supplemental Figure 3)

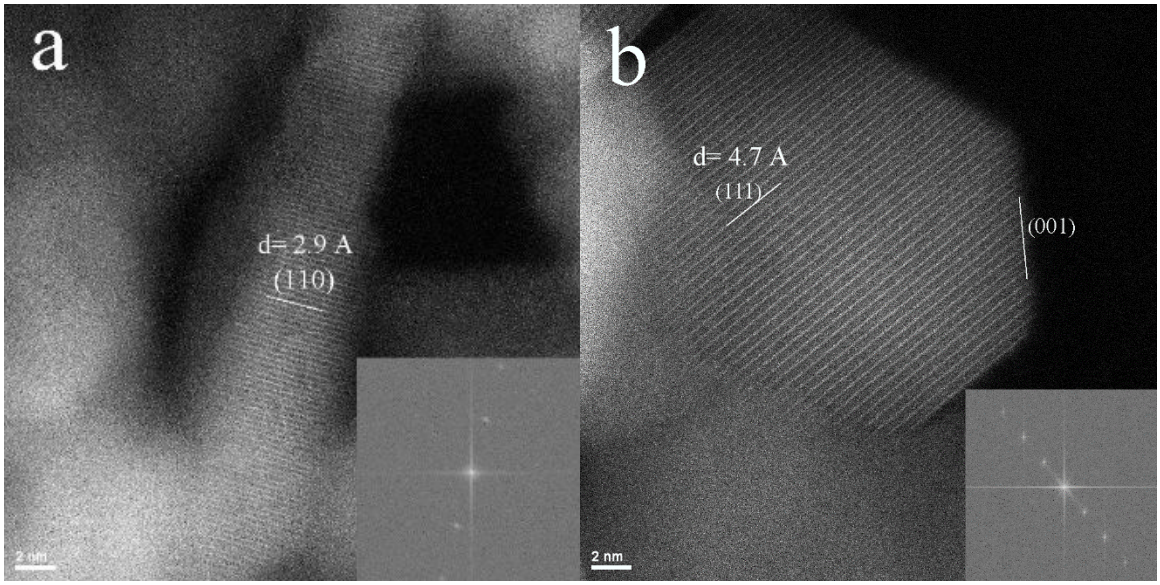

Figure 3. Aberration corrected-scanning transmission electron microscope images of a) Co nanorods and b) nanoparticles. The insets show the corresponding Fast Fourier Transforms. Scale bar is 2 nm

3.4 in situ CO_2 hydrogenation DRIFTS spectroscopy

Differences in surface crystal facets on the Co nanorods and nanoparticles is expected to result in distinct catalytic activity, particularly for a structure sensitive reaction such as CO_2 hydrogenation.[11-15, 17, 18] *In situ* IR spectroscopy was applied to study surface reactive species during CO_2 hydrogenation on both the Co nanorods and nanoparticles. Reaction temperatures and the reductive pretreatment were identical to those set in the plug-flow reactor. The *in situ* IR spectra under steady-state reaction conditions are shown in Fig. 4. The formation of formyl (H-C=O*) species at 1700 cm^{-1} was observed on both Co nanorods and nanoparticles. In contrast, formate species (HCOO*, bands at 1600 cm^{-1} and 1415 cm^{-1}) were only formed on the Co nanoparticles. Formate has previously been reported as an inactive species for CO_2 hydrogenation,[35-38] thus blocking catalytically active sites. For PtCo based catalyst, the direct hydrogenation of CO_2 to form *HCOO is kinetically unfavorable (ΔE=-0.25 eV), while the formation of a *HOCO reactive intermediate (ΔE=-0.56 eV) is more energetically favorable.[38]

The *HOCO intermediate can further dissociate into *CO and *OH, where the *CO undergoes another hydrogenation step to form *HCO and the adsorbed *OH is hydrogenated to form water.[38] Formate has been reported as a reactive intermediate for the production of methanol over Cu/ZnO,[39] however for methanation formate is generally considered a spectator species,[35-38] which is consistent with our experimental findings. Furthermore, in the case of nickel based catalyst, CO_2 is also believed to undergo a dissociation step, however, the resulting adsorbed CO further dissociated to adsorbed C and O which are then hydrogenated to form methane and water; respectively, where formate was also observed as a spectator species.[40] To probe the formation of the site blocking formate species on both catalysts, room temperature adsorption of CO_2 and CO was performed, as shown in Fig. 5. Both catalyst formed bidentate- and unidentate-carbonates (1650, 1540, 1293, and 1032 cm^{-1}),[41] but only the nanoparticles showed the formation of formate species. Bidentate- and unidentate-carbonates are typically less stable than formate,[42] which explains why only formate species can be observed during *in situ* IR reaction experiments conducted at 250 °C.

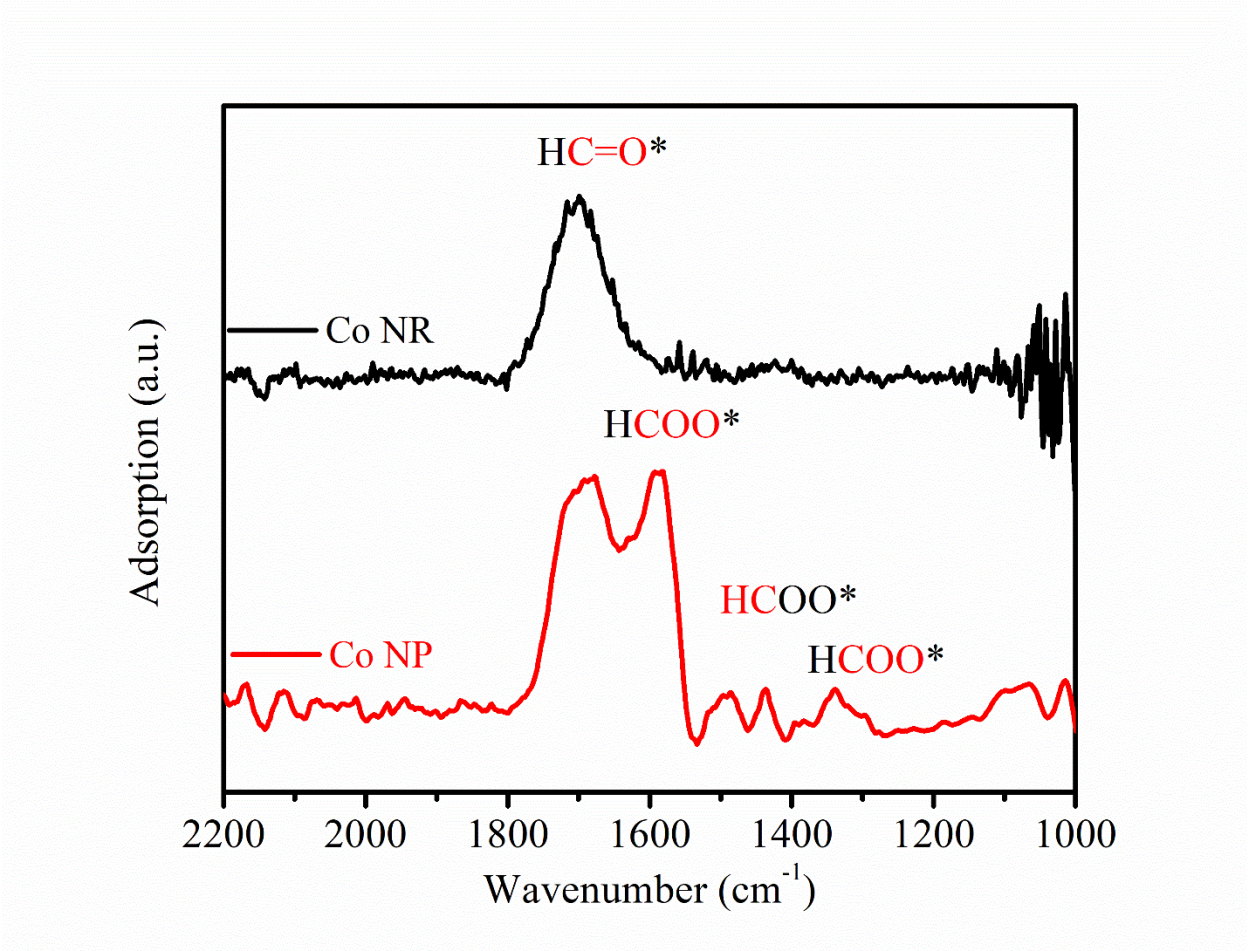

Figure 4. *in situ* IR of CO_2 hydrogenation on nanorods and nanoparticles at 250°C.

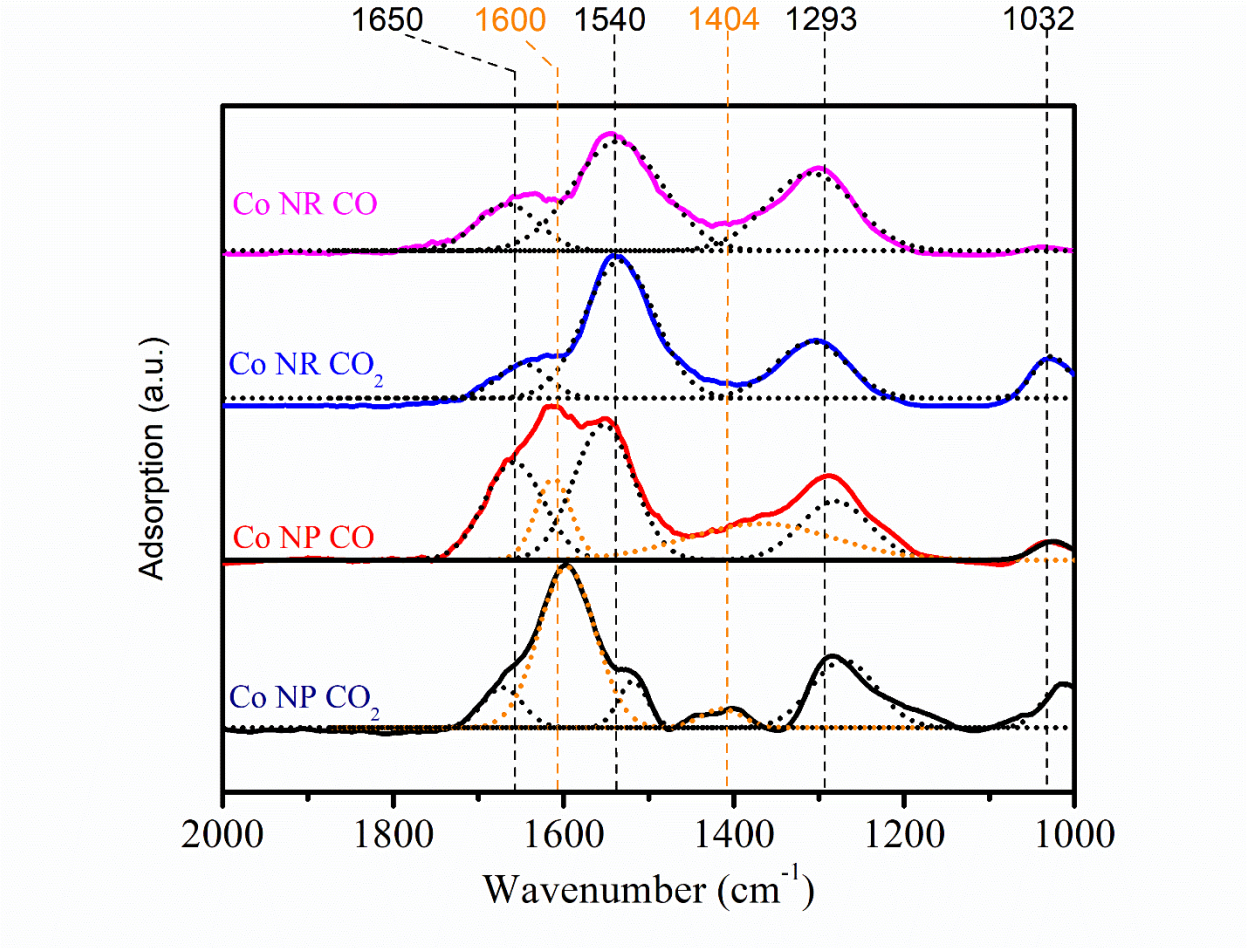

Figure 5. IR spectra of CO_2 and CO adsorption on nanorods and nanoparticles at room temperature. The formate species located at 1600 and 1293 cm^{-1} are fitted with orange dot lines, and carbonate species (1650, 1540, 1293, and 1032 cm^{-1}) are fitted with black dot curves

The site-blocking role of formate species on the surface of the Co nanoparticles is also supported by CO_2-Temperature Programmed Desorption (TPD) results (supplemental Fig. 4). Both catalysts have a CO_2 desorption peak at 80 ^oC, while the nanoparticles show an additional CO_2 desorption peak at 175 ^oC. The lower temperature peak can be attributed to the desorption of the bidentate carbonate species, while the higher temperature peak on the Co nanoparticles can be assigned to the desorption of the formate species.[42, 43] This further validates that formate species are acting as a spectator to the reaction, limiting the total number of active sites for the reaction. To understand the nature of the active sites, the apparent activation energies for CO_2

hydrogenation on both nanorods and nanoparticles were calculated based on the Arrhenius equation. The resulting energies are nearly identical at 87.5 ± 4 and 81.6 ± 7 kJ/mol (supplemental Fig. 5); respectively. Additionally, since the presence of sodium as a remainder from the synthesis procedure has been shown to promote hydrogenation reactions,[44-46] an X-Ray Photoelectron survey scan was performed before and after washing the catalyst and found no presence of the Na 1s peak at 1070 eV, ruling out the influence of sodium on the catalytic activity (supplemental Fig. 6).

3.5 Effective surface area and turnover frequency

To further elucidate the catalytic surface, chemisorption and physisorption were employed to determine the number of active sites and the surface area of the catalyst; respectively. Table 1 shows the surface area and the chemisorbed CO uptake of both the Co nanorods and Co nanoparticles as well as the CO_2 turnover frequency (TOF) at 220°C. The nanorods had a surface area of 196 ± 14 m^2/g while the nanoparticles had a surface area of 155 ± 22 m^2/g. Furthermore, upon reduction under the same reaction pretreatment conditions, the fresh Co nanoparticles possess a comparable number of active sites as the Co nanorods. CO chemisorption on the nanorods yielded an uptake of (0.97 ± 0.08) $x10^{-2}$ $mmol_{CO}/g_{cat}$, while the nanoparticles had an uptake of (1.09 ± 0.12) $x10^{-2}$ $mmol_{CO}/g_{cat}$, showing the number of active sites on both catalysts are within error of each other; ruling out the possibility of the presence of more active sites on the nanorods being the cause for the difference in catalytic activity. This is captured in the turnover frequency (TOF), where the rate of CO_2 ($mol_{CO2}\cdot g^{-1}\cdot s^{-1}$) conversion was normalized by the total number of active sites measured via CO chemisorption (mol_{CO}/g_{cat}). At a temperature of 220°C, the nanorods possess an order of magnitude higher TOF than the nanoparticles, where the nanoparticles show a comparable TOF to that which is reported in the

literature for spherical cobalt nanoparticles for CO_2 hydrogenation.[17] The difference between the two catalyst can be further exemplified if the TOF of methane as opposed to the TOF of CO_2 is considered, where the nanorods have a factor of 5 greater selectivity towards methane at 220°C than the nanoparticles. These results coupled with the comparable activation energy of both the nanorods and nanoparticles further confirm that site-blocking by formate species under reaction condition is the cause of lower activity on nanoparticles instead of smaller surface area or lower number of active sites on fresh catalysts.

Table 1: Total surface area, amount of available surface sites, and the CO_2 turnover frequency at 220°C for both catalyst

Sample	***Surface Area (m^2/g_{cat})***	***CO Uptake ($mmol_{CO}/g_{cat}$)***	***TOF-220°C (s^{-1})***
CoNR	196 ± 14	(0.97 ± 0.08) x10^{-2}	2.89
CoNP	155 ± 22	(1.09 ± 0.12) x10^{-2}	0.361

3.6 CO hydrogenation mechanism on nanorods and nanoparticles

Aside from the higher catalytic activity, the Co nanorods also have substantially higher selectivity towards methane if compared to the nanoparticles (see Figure 1). The hydrogenation mechanism follows a two-step reactions scheme.[3, 9, 32] First, CO_2 is partially hydrogenated into CO, which is then further hydrogenated in a second step to form methane. The second hydrogenation step ($CO + 3H_2 \rightarrow CH_4 + H_2O$) is widely reported as the rate-determining step for methane production,[3, 30] and thus should determine the selectivity to CO and methane in the overall CO_2 hydrogenation process. To investigate the selectivity differences observed between the Co nanorods and nanoparticles, reactive intermediates were studied by using *in situ* CO

hydrogenation (second hydrogenation step) as a model reaction, see Fig. 6. It is expected for reactive intermediates to quickly respond to changes in the gas phase environment, while the response of spectator species will be considerably slower.[47] The IR intensity of chemisorbed CO (bands above 1650 cm^{-1}) remains mostly constant during reaction, while that of carbonate bands (below 1650 cm^{-1}, bidentate and unidentate) increases with time on-stream. Thus, the IR spectra confirm that chemisorbed CO is a reactive intermediate, while the carbonates are spectator species, which is consistent with the CO hydrogenation literature.[48] More interestingly, while both nanorods and nanoparticles have CO chemisorbed in hollow sites (band at 1760 cm^{-1}), the nanorods show an additional band corresponding to CO chemisorbed on a bridge site (1900 cm^{-1}). The presence of these extra sites on the Co nanorods is corroborated via CO-TPD (supplemental Fig. 7) where an extra CO desorption peak was detected around 115 ^{o}C. This CO desorption peak can be attributed to the desorption of bridge site CO,[49, 50] while the carbonate and hollow site chemisorbed CO species are desorbing in the form of CO_2 at higher temperatures. Bridge site CO was reported to have higher hydrogenation activity compared with hollow site CO, and will in-turn promote methane production.[51-53] In summary, the *in situ* IR spectra and TPD profiles show bridge-site CO intermediates with higher activity on the nanorods, which facilitates the production of methane.

3.7 Preferential crystallographic growth

To understand differences in surface species present on the reduced Co nanorods and nanoparticles during CO_2 hydrogenation, the IR spectra of CO adsorption shown in Fig. 5 were found to be comparable to those reported for CO adsorption on stepped {10-12} and flat {0001} surfaces; respectively.[52] CO prefers to adsorb and dissociate on both bridge and hollow sites on stepped Co surfaces, but prefers atop or hollow sites on flat Co surfaces.[52, 53] During our *in*

situ IR experiments, the Co nanorods showed CO adsorbed on both bridge and hollow sites, while the nanoparticles showed only hollow site CO. Furthermore, the stepped surfaces have a lower activation energy of 160.9 kJ/mol for CO dissociation than the 220 kJ/mol required on the flat surface, leading to higher activity for CO hydrogenation.[52] This is consistent with our CO_2 hydrogenation results on the Co nanorods, which demonstrated higher activity for CO_2 hydrogenation than the Co nanoparticles. The stepped {10-12} and the flat {0001} Co planes can be expected to form epitaxially on the Co nanorods and nanoparticles surfaces during catalyst reduction due to the similarity between their lattice parameters. The lattice mismatch between facet groups of Co_3O_4 {110} and Co {10-12} is less than 5%, and it is less than 2% between Co_3O_4 {001} and Co {0001} planes. A formation of Co {0001} planes on Co_3O_4 {110}, on the other side, will lead to a lattice mismatch of 39%, which represents a significant energy penalty for non-epitaxial growth of reduced Co. Furthermore, the formation of Co {111} planes on Co_3O_4{111} has been proven previously via environmental HRTEM during the H_2 reduction of model Co_3O_4 catalysts.[54] A similar reduction process was performed here for Co nanorods and nanoparticles before CO_2 hydrogenation. As both the nanorods and the nanoparticles share the {001} family of surface facets, the observed differences in the surface species on both catalyst is attributed to the different surface structures present on the reduced form of the {110} family of surface facets, while the reduced form of the {111} family of surface present on the nanoparticles resulted in the presence of both the reactive intermediate as well as the spectator species. The comparison of our results with literature suggests that the Co nanorods and nanoparticles have distinct active Co surfaces exposed during CO_2 hydrogenation, where the metallic Co surface that arises from the reduction of the {110}/{001} based nanorod ultimately leads to the suppression of the site blocking species and promotes the exclusive formation of the reactive intermediate. Ultimately, by mitigating spectator species via the tuning of the exposed surface facets of the cobalt oxide, we have developed a highly

active catalyst; where the performance of the catalyst in this study are compared to some of the state-of-the-art catalyst in literature,[9, 17, 38, 55-57] shown in Table S1. However, it should be noted that due to the inherent difference in operating conditions (such as pressure and temperature) a direct comparison with literature is not feasible.

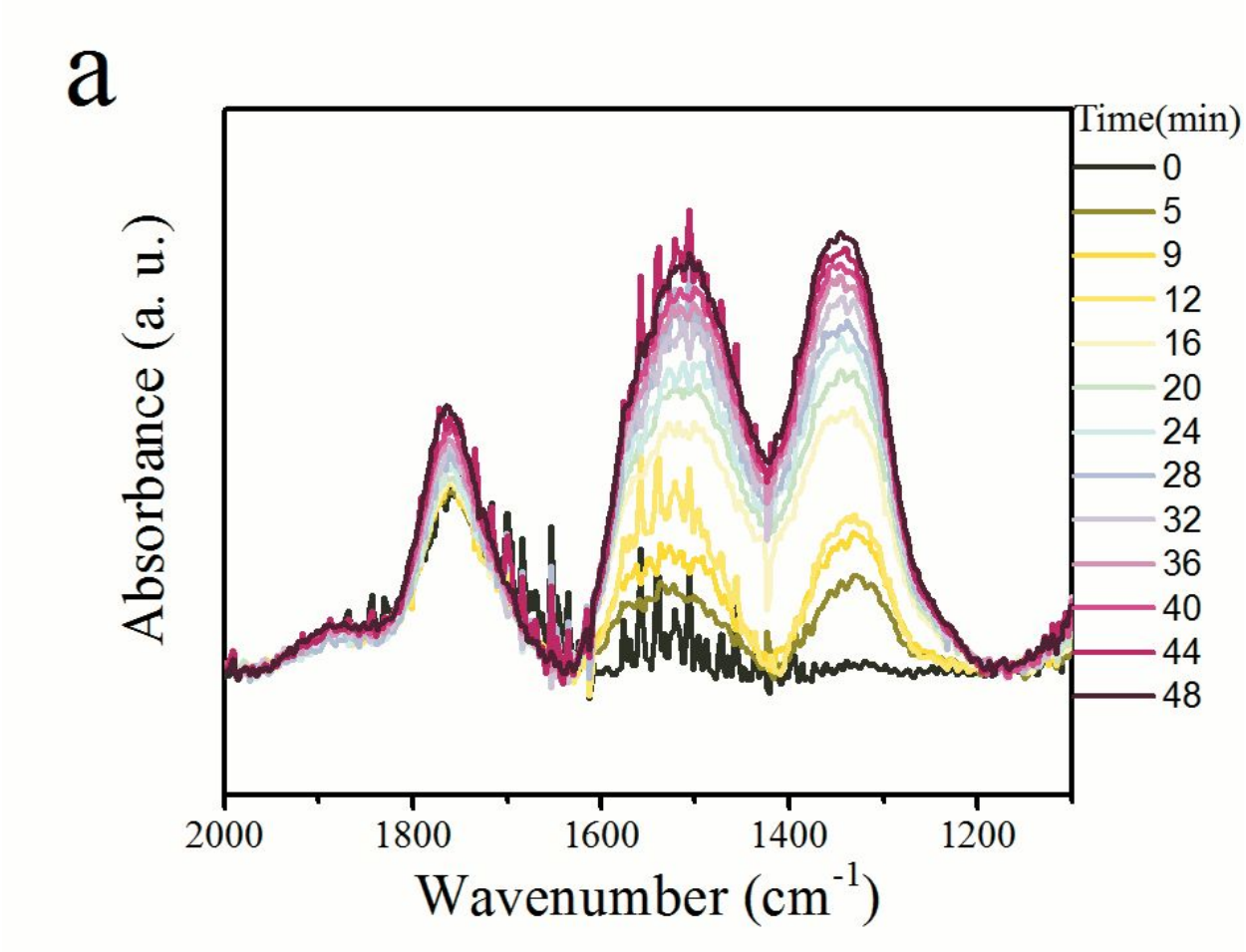

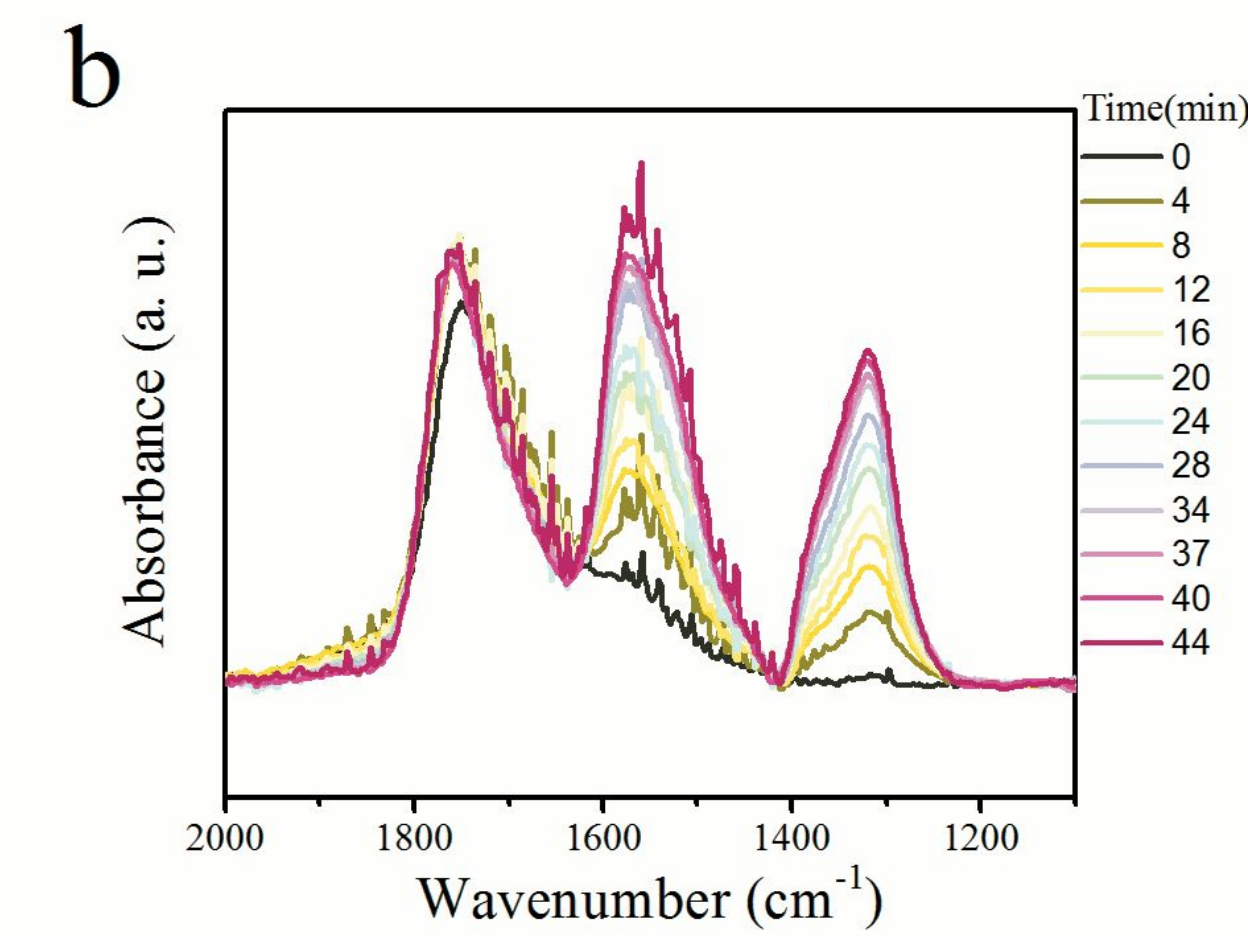

Figure 6. *In situ* IR of CO hydrogenation on a) nanorods and b) nanoparticles at 250°C.

3.8 Lifetime study and in situ Raman

Since Co catalyst are very susceptible to oxidation and subsequently deactivate,[25-27] CO_2 hydrogenation activity was tested under reaction conditions for 50 hours. The results are shown in Figure 7 and no change in selectivity was observed. Additionally, the CO_2 conversion remained at a constant 70% throughout the entire testing period. This suggests the catalyst did not undergo deactivation, which could arise from either oxidation of the catalyst due to the water produced via the hydrogenation or by the formation of coke,[9, 26, 27] which would deposit onto the active sites and lower the activity and selectivity towards methane. The oxidation state of the catalyst was observed during CO_2 hydrogenation after a reduction at 450°C under

hydrogen for the Co nanoparticles (supplemental Fig 8), where metallic cobalt is Raman inactive. There was no observed formation of the cobalt oxide phase at 680, 450 or 200 cm^{-1}, which would be attributed to the formation of either the spinel Co_3O_4, rocksalt CoO, or the CoOOH hydroxide structure.[58, 59] The shift in selectivity from predominantly CO to methane was believed to be due to the formation of a surface oxide, however no oxidation was observed. As no change in selectivity was observed for the cobalt nanorods the *in situ* Raman was not carried out on the Co nanorods. Deactivation via coke formation was also ruled by post reaction Raman spectroscopy, where the absence of D and G bands at 1340 and 1580 cm^{-1}, respectively, demonstrated that no carbon was deposited onto the catalyst, which can occur via CO disproportionation.[60]

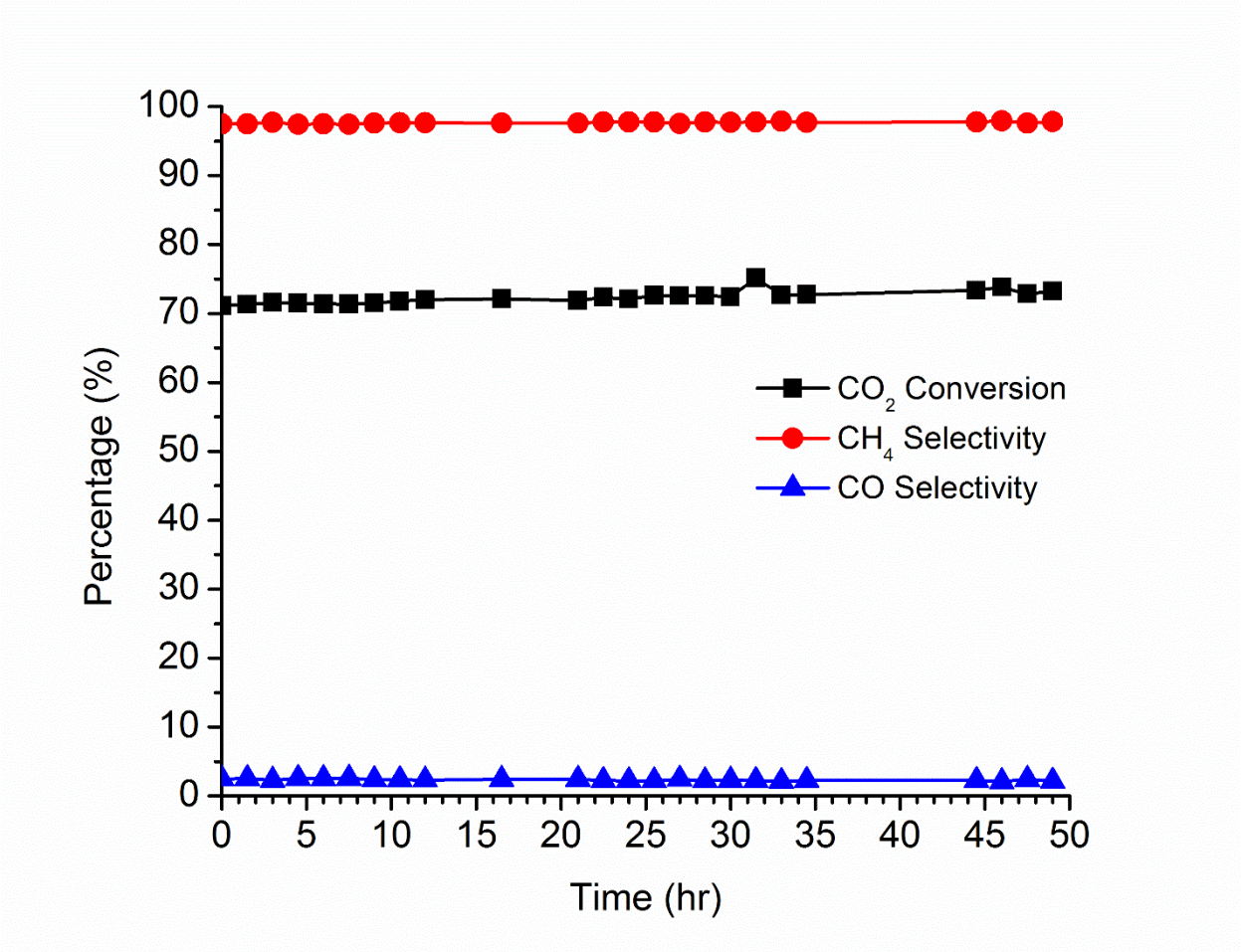

Figure 7. Time on stream study for Cobalt nanorods at 230°C, 10bar, 4:1 ratio of H_2 to CO_2 and a flow rate of 18000 hr^{-1}

4. Conclusions

In summary, we have demonstrated that tuning the catalyst surface structures on cobalt via control of nanoscale morphology is an efficient way to design active catalysts by suppressing the formation of site-blocking surface intermediates. This is accomplished by selectively exposing different crystallographic facets on the active catalyst surface, while maintaining similar bulk properties, including particle size, crystallographic structure, chemical composition, and oxidation state. CO_2 hydrogenation tests show that Co nanorods that are synthesized as Co_3O_4 precursors with exposed {110} surface facets have substantially

improved catalytic activity and selectivity towards methane than nanoparticles from Co_3O_4 precursors with exposed {111} and {001} facets. The superior activity of Co nanorods results from a suppression of site-blocking formate species. The greater methane selectivity on the nanorods is attributed to the more active bridge-site CO as the reactive intermediate for methane formation. The catalyst reported here also requires less energy for the large-scale conversion of CO_2 to hydrocarbons, making the process more efficient and sustainable.

Acknowledgements

Financial support from the South Carolina Center of Economic Excellence for Strategic Approaches to the Generation of Electricity is highly appreciated as well as support from the US National Science Foundation, grants DGE 1250052 and EEC 1358931. We thank Jason Hattrick-Simpers and Kathleen Mingle for their input during discussions.

Keywords: CO_2 Hydrogenation, nanostructures, cobalt catalyst, surface intermediates, in situ DRIFTS

References

1. M. Mikkelsen, M. Jorgensen and F. C. Krebs, *Energ Environ Sci*, 2010, **3**, 43-81.
2. S. L. Suib, *Activation of Carbon Dioxide*, Elsevier Science, Waltham, MA 02451, USA, 2013.
3. W. Wang, S. Wang, X. Ma and J. Gong, *Chemical Society reviews*, 2011, **40**, 3703-3727.
4. J. Gibbins and H. Chalmers, *Energy Policy*, 2008, **36**, 4317-4322.
5. P. J. Lunde and F. L. Kester, *Industrial & Engineering Chemistry Process Design and Development*, 1974, **13**, 27-33.

6. J. A. Dumesic, *The Microkinetics of Heterogeneous Catalysis*, American Chemical Society, Washington, DC, 1993.
7. J. Ma, N. Sun, X. Zhang, N. Zhao, F. Xiao, W. Wei and Y. Sun, *Catal Today*, 2009, **148**, 221-231.
8. D. Kim, J. Resasco, Y. Yu, A. M. Asiri and P. Yang, *Nat Commun*, 2014, **5**.
9. J. Wu, C. Wen, X. Zou, J. Jimenez, J. Sun, Y. Xia, M.-T. Fonseca Rodrigues, S. Vinod, J. Zhong, N. Chopra, I. N. Odeh, G. Ding, J. Lauterbach and P. M. Ajayan, *ACS Catalysis*, 2017, **7**, 4497-4503.
10. A. V. Puga, *Catalysis Science & Technology*, 2018, **8**, 5681-5707.
11. S. K. Beaumont, S. Alayoglu, C. Specht, W. D. Michalak, V. V. Pushkarev, J. H. Guo, N. Kruse and G. A. Somorjai, *Journal of the American Chemical Society*, 2014, **136**, 9898-9901.
12. G. Melaet, W. T. Ralston, C. S. Li, S. Alayoglu, K. An, N. Musselwhite, B. Kalkan and G. A. Somorjai, *Journal of the American Chemical Society*, 2014, **136**, 2260-2263.
13. W. L. Zhen, B. Li, G. X. Lu and J. T. Ma, *Rsc Advances*, 2014, **4**, 16472-16479.
14. S. Tada, O. J. Ochieng, R. Kikuchi, T. Haneda and H. Kameyama, *International Journal of Hydrogen Energy*, 2014, **39**, 10090-10100.
15. Q. S. Pan, J. X. Peng, T. J. Sun, S. Wang and S. D. Wang, *Catalysis Communications*, 2014, **45**, 74-78.
16. P. J. Dauenhauer, B. J. Dreyer, N. J. Degenstein and L. D. Schmidt, *Angewandte Chemie-International Edition*, 2007, **46**, 5864-5867.
17. V. Iablokov, S. K. Beaumont, S. Alayoglu, V. V. Pushkarev, C. Specht, J. Gao, A. P. Alivisatos, N. Kruse and G. A. Somorjai, *Nano Letters*, 2012, **12**, 3091-3096.
18. J. P. den Breejen, P. B. Radstake, G. L. Bezemer, J. H. Bitter, V. Frøseth, A. Holmen and K. P. d. Jong, *J Am Chem Soc*, 2009, **131**, 7197-7203.
19. F. Tao, M. E. Grass, Y. W. Zhang, D. R. Butcher, J. R. Renzas, Z. Liu, J. Y. Chung, B. S. Mun, M. Salmeron and G. A. Somorjai, *Science*, 2008, **322**, 932-934.
20. Y. Zhu, S. Zhang, Y. Ye, X. Zhang, L. Wang, W. Zhu, F. Cheng and F. Tao, *ACS Catalysis*, 2012, **2**, 2403-2408.
21. D. I. Enache, B. Rebours, M. Roy-Auberger and R. Revel, *Journal of Catalysis*, 2002, **205**, 346-353.
22. W. K. Jozwiak, E. Szubiakiewicz, J. Goralski, A. Klonkowski and T. Paryjczak, *Kinet Catal+*, 2004, **45**, 247-255.
23. J. Lahtinen, T. Anraku and G. A. Somorjai, *Catal Lett*, 1994, **25**, 241-255.
24. Y. Q. Zhang, G. Jacobs, D. E. Sparks, M. E. Dry and B. H. Davis, *Catal Today*, 2002, **71**, 411-418.
25. J. Jimenez, A. Bird, M. Santos Santiago, C. Wen and J. Lauterbach, *Energy Technology*, 2017, **5**, 884-891.
26. C. Wen, D. Dunbar, X. Zhang, J. Lauterbach and J. Hattrick-Simpers, *Chemical Communications*, 2014, **50**, 4575-4578.
27. X. W. Xie, Y. Li, Z. Q. Liu, M. Haruta and W. J. Shen, *Nature*, 2009, **458**, 746-749.
28. X. Xie, P. Shang, Z. Liu, Y. Lv, Y. Li and W. Shen, *The Journal of Physical Chemistry C*, 2010, **114**, 2116-2123.
29. G. Weatherbee, *Journal of Catalysis*, 1982, **77**, 460-472.
30. G. D. Weatherbee and C. H. Bartholomew, *J Catal*, 1984, **87**, 352-362.
31. B. Miao, S. S. K. Ma, X. Wang, H. Su and S. H. Chan, *Catal. Sci. Technol.*, 2016, **6**, 4048-4058.
32. W. Wei and G. Jinlong, *Front. Chem. Sci. Eng.*, 2011, **5**, 2-10.
33. I. Ghampson, C. Newman, L. Kong, E. Pier, K. Hurley, R. Pollock, B. Walsh, B. Goundie, J. Wright and M. Wheeler, *Applied Catalysis A: General*, 2010, **388**, 57-67.
34. N. Srisawad, W. Chaitree, O. Mekasuwandumrong, A. Shotipruk, B. Jongsomjit and J. Panpranot, *Reac Kinet Mech Cat*, 2012, **107**, 179-188.
35. T. Das and G. Deo, *Journal of Molecular Catalysis A: Chemical*, 2011, **350**, 75-82.
36. T. Das and G. Deo, *Catalysis Today*, 2012, **198**, 116-124.

37. T. Das and G. Deo, *The Journal of Physical Chemistry C*, 2012, **116**, 20812-20819.
38. S. Kattel, W. Yu, X. Yang, B. Yan, Y. Huang, W. Wan, P. Liu and J. G. Chen, *Angewandte Chemie*, 2016, **128**, 8100-8105.
39. S. Kattel, P. J. Ramírez, J. G. Chen, J. A. Rodriguez and P. Liu, *Science*, 2017, **355**, 1296-1299.
40. J. Y. Lim, J. McGregor, A. Sederman and J. Dennis, *Chemical Engineering Science*, 2016, **141**, 28-45.
41. C. G. Visconti, L. Lietti, E. Tronconi, P. Forzatti, R. Zennaro and E. Finocchio, *Applied Catalysis A: General*, 2009, **355**, 61-68.
42. C. Li, Y. Sakata, T. Arai, K. Domen, K.-i. Maruya and T. Onishi, *Journal of the Chemical Society, Faraday Transactions 1: Physical Chemistry in Condensed Phases*, 1989, **85**, 929-943.
43. G. Li, M. Ridd and F. Larkins, *Australian Journal of Chemistry*, 1991, **44**, 623-626.
44. M. Dry, T. Shingles and C. v. H. Botha, *Journal of Catalysis*, 1970, **17**, 341-346.
45. B. Liang, T. Sun, J. Ma, H. Duan, L. Li, X. Yang, Y. Zhang, X. Su, Y. Huang and T. Zhang, *Catalysis Science & Technology*, 2019, **9**, 456-464.
46. M. K. Gnanamani, G. Jacobs, R. A. Keogh, W. D. Shafer, D. E. Sparks, S. D. Hopps, G. A. Thomas and B. H. Davis, *Applied Catalysis A: General*, 2015, **499**, 39-46.
47. S. Eckle, H.-G. Anfang and R. J. r. Behm, *The Journal of Physical Chemistry C*, 2010, **115**, 1361-1367.
48. J. P. Hindermann, G. J. Hutchings and A. Kiennemann, *Catalysis Reviews*, 1993, **35**, 1-127.
49. A. F. Carlsson, M. Naschitzki, M. Bäumer and H. J. Freund, *The Journal of Physical Chemistry B*, 2003, **107**, 778-785.
50. J. Lahtinen, J. Vaari and K. Kauraala, *Surf Sci*, 1998, **418**, 502-510.
51. J. Cheng, X.-Q. Gong, P. Hu, C. M. Lok, P. Ellis and S. French, *J Catal*, 2008, **254**, 285-295.
52. Q. Ge and M. Neurock, *The Journal of Physical Chemistry B*, 2006, **110**, 15368-15380.
53. J.-X. Liu, H.-Y. Su, D.-P. Sun, B.-Y. Zhang and W.-X. Li, *Journal of the American Chemical Society*, 2013, **135**, 16284-16287.
54. D. Potoczna-Petru and L. Kępiński, *Catal Lett*, 2001, **73**, 41-46.
55. T. Abe, M. Tanizawa, K. Watanabe and A. Taguchi, *Energy & Environmental Science*, 2009, **2**, 315-315.
56. P. U. Aldana, F. Ocampo, K. Kobl, B. Louis, F. Thibault-Starzyk, M. Daturi, P. Bazin, S. Thomas and A. Roger, *Catalysis Today*, 2013, **215**, 201-207.
57. J. H. Kwak, L. Kovarik and J. Szanyi, *ACS Catalysis*, 2013, **3**, 2449-2455.
58. T. Pauporté, L. Mendoza, M. Cassir, M. C. Bernard and J. Chivot, *Journal of The Electrochemical Society*, 2005, **152**, C49-C49.
59. J. Yang, H. Liu, W. N. Martens and R. L. Frost, *The Journal of Physical Chemistry C*, 2010, **114**, 111-119.
60. S. A. Chernyak, E. V. Suslova, A. V. Egorov, K. I. Maslakov, S. V. Savilov and V. V. Lunin, *Applied Surface Science*, 2016, **372**, 100-107.

Catalyst design by tuning surface structures to suppress unreactive species in order to achieve higher reactivity for CO_2 conversion.

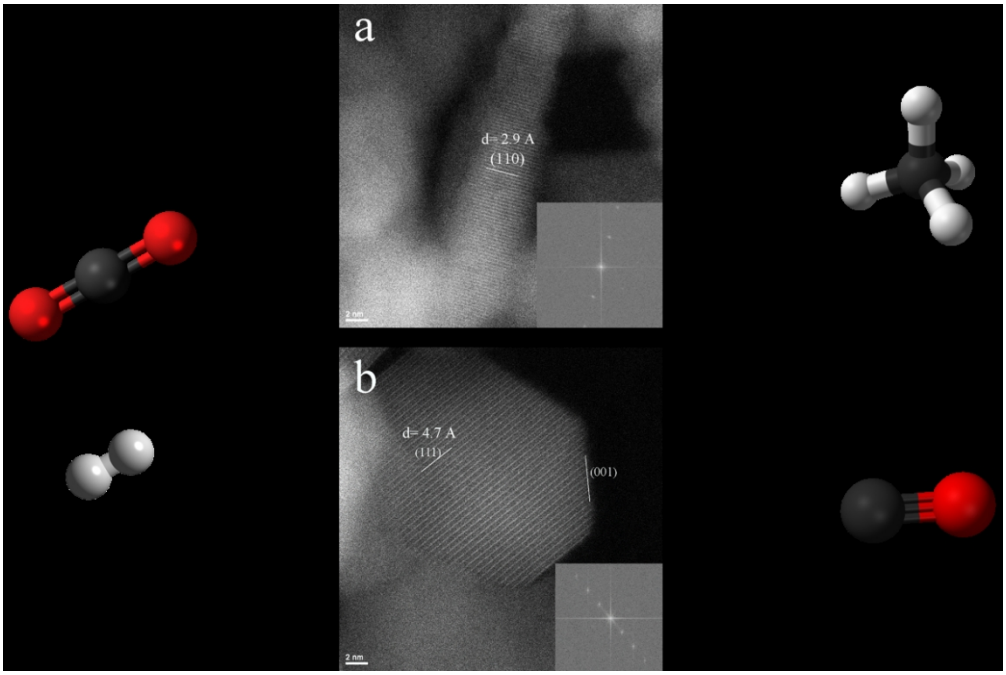

200x133mm (150 x 150 DPI)